



X-Ray Polarized View of the Accretion Geometry in the X-Ray Binary Circinus X-1

John Rankin¹, Fabio La Monaca^{1,2,3}, Alessandro Di Marco¹, Juri Poutanen⁴, Anna Bobrikova⁴, Vadim Kravtsov⁴, Fabio Muleri¹, Maura Pilia⁵, Alexandra Vedula^{4,6}, Rob Fender⁷, Philip Kaaret⁸, Dawoon E. Kim^{1,2,3}, Andrea Marinucci⁹, Herman L. Marshall¹⁰, Alessandro Papitto¹¹, Allyn F. Tennant⁸, Sergey S. Tsygankov⁴, Martin C. Weisskopf⁸, Kinwah Wu¹², Silvia Zane¹², Filippo Ambrosino¹¹, Ruben Farinelli¹³, Andrea Gnarini¹⁴, Iván Agudo¹⁵, Lucio A. Antonelli^{11,16}, Matteo Bachetti⁵, Luca Baldini^{17,18}, Wayne H. Baumgartner⁸, Ronaldo Bellazzini¹⁷, Stefano Bianchi¹⁴, Stephen D. Bongiorno⁸, Raffaella Bonino^{19,20}, Alessandro Brez¹⁷, Niccolò Bucciantini^{21,22,23}, Fiamma Capitanio¹, Simone Castellano¹⁷, Elisabetta Cavazzuti⁹, Chien-Ting Chen²⁴, Stefano Ciprini^{16,25}, Enrico Costa¹, Alessandra De Rosa¹, Ettore Del Monte¹, Laura Di Gesu⁹, Niccolò Di Lalla²⁶, Immacolata Donnarumma⁹, Victor Doroshenko²⁷, Michal Dovčiak²⁸, Steven R. Ehlert⁸, Teruaki Enoto²⁹, Yuri Evangelista¹, Sergio Fabiani¹, Riccardo Ferrazzoli¹, Javier A. Garcia³⁰, Shuichi Gunji³¹, Kiyoshi Hayashida^{32,53}, Jeremy Heyl³³, Wataru Iwakiri³⁴, Svetlana G. Jorstad^{35,36}, Vladimir Karas²⁸, Fabian Kislak³⁷, Takao Kitaguchi²⁹, Jeffery J. Kolodziejczak⁸, Henric Krawczynski³⁸, Luca Latronico¹⁹, Ioannis Liodakis⁸, Simone Maldera¹⁹, Alberto Manfreda³⁹, Frédéric Marin⁴⁰, Alan P. Marscher³⁵, Francesco Massaro^{19,20}, Giorgio Matt¹⁴, Ikuyuki Mitsuishi⁴¹, Tsunefumi Mizuno⁴², Michela Negro⁴³, Chi-Yung Ng⁴⁴, Stephen L. O'Dell⁸, Nicola Omodei²⁶, Chiara Oppedisano¹⁹, George G. Pavlov⁴⁵, Abel L. Peirson²⁶, Matteo Perri^{11,16}, Melissa Pesce-Rollins¹⁷, Pierre-Olivier Petrucci⁴⁶, Andrea Possenti⁵, Simonetta Puccetti¹⁶, Brian D. Ramsey⁸, Ajay Ratheesh¹, Oliver J. Roberts²⁴, Roger W. Romani²⁶, Carmelo Sgrò¹⁷, Patrick Slane⁴⁷, Paolo Soffitta¹, Gloria Spandre¹⁷, Douglas A. Swartz²⁴, Toru Tamagawa²⁹, Fabrizio Tavecchio⁴⁸, Roberto Taverna⁴⁹, Yuzuru Tawara⁴¹, Nicholas E. Thomas⁸, Francesco Tombesi^{2,25,50}, Alessio Trois⁵, Roberto Turolla^{12,49}, Jacco Vink⁵¹, and Fei Xie^{1,52}

¹ INAF Istituto di Astrofisica e Planetologia Spaziali, Via del Fosso del Cavaliere 100, I-00133 Roma, Italy

² Dipartimento di Fisica, Università degli Studi di Roma "Tor Vergata," Via della Ricerca Scientifica 1, I-00133 Roma, Italy

³ Dipartimento di Fisica, Università degli Studi di Roma "La Sapienza," Piazzale Aldo Moro 5, I-00185 Roma, Italy

⁴ Department of Physics and Astronomy, 20014 University of Turku, Finland

⁵ INAF Osservatorio Astronomico di Cagliari, Via della Scienza 5, I-09047 Selargius (CA), Italy

⁶ Nordita, KTH Royal Institute of Technology and Stockholm University, Hannes Alfvéns väg 12, SE-106 91, Sweden

⁷ Department of Physics, University of Oxford, Denys Wilkinson Building, Keble Road, Oxford OX1 3RH, UK

⁸ NASA Marshall Space Flight Center, Huntsville, AL 35812, USA

⁹ Agenzia Spaziale Italiana, Via del Politecnico snc, I-00133 Roma, Italy

¹⁰ MIT Kavli Institute for Astrophysics and Space Research, Massachusetts Institute of Technology, 77 Massachusetts Avenue, Cambridge, MA 02139, USA

¹¹ INAF Osservatorio Astronomico di Roma, Via Frascati 33, I-00040 Monte Porzio Catone (RM), Italy

¹² Mullard Space Science Laboratory, University College London, Holmbury St Mary, Dorking, Surrey RH5 6NT, UK

¹³ INAF Osservatorio di Astrofisica e Scienza dello Spazio di Bologna, Via P. Gobetti 101, I-40129 Bologna, Italy

¹⁴ Dipartimento di Matematica e Fisica, Università degli Studi Roma Tre, Via della Vasca Navale 84, I-00146 Roma, Italy

¹⁵ Instituto de Astrofísica de Andalucía—CSIC, Glorieta de la Astronomía s/n, E-18008 Granada, Spain

¹⁶ Space Science Data Center, Agenzia Spaziale Italiana, Via del Politecnico snc, I-00133 Roma, Italy

¹⁷ Istituto Nazionale di Fisica Nucleare, Sezione di Pisa, Largo B. Pontecorvo 3, I-56127 Pisa, Italy

¹⁸ Dipartimento di Fisica, Università di Pisa, Largo B. Pontecorvo 3, I-56127 Pisa, Italy

¹⁹ Istituto Nazionale di Fisica Nucleare, Sezione di Torino, Via Pietro Giuria 1, I-10125 Torino, Italy

²⁰ Dipartimento di Fisica, Università degli Studi di Torino, Via Pietro Giuria 1, I-10125 Torino, Italy

²¹ INAF Osservatorio Astrofisico di Arcetri, Largo Enrico Fermi 5, I-50125 Firenze, Italy

²² Dipartimento di Fisica e Astronomia, Università degli Studi di Firenze, Via Sansone 1, I-50019 Sesto Fiorentino (FI), Italy

²³ Istituto Nazionale di Fisica Nucleare, Sezione di Firenze, Via Sansone 1, I-50019 Sesto Fiorentino (FI), Italy

²⁴ Science and Technology Institute, Universities Space Research Association, Huntsville, AL 35805, USA

²⁵ Istituto Nazionale di Fisica Nucleare, Sezione di Roma "Tor Vergata," Via della Ricerca Scientifica 1, I-00133 Roma, Italy

²⁶ Department of Physics and Kavli Institute for Particle Astrophysics and Cosmology, Stanford University, Stanford, CA 94305, USA

²⁷ Institut für Astronomie und Astrophysik, Universität Tübingen, Sand 1, D-72076 Tübingen, Germany

²⁸ Astronomical Institute of the Czech Academy of Sciences, Boční II 1401/1, 14100 Praha 4, Czech Republic

²⁹ RIKEN Cluster for Pioneering Research, 2-1 Hirosawa, Wako, Saitama 351-0198, Japan

³⁰ NASA Goddard Space Flight Center, Greenbelt, MD 20771, USA

³¹ Yamagata University, 1-4-12 Kojirakawa-machi, Yamagata-shi 990-8560, Japan

³² Osaka University, 1-1 Yamadaoka, Suita, Osaka 565-0871, Japan

³³ University of British Columbia, Vancouver, BC V6T 1Z4, Canada

³⁴ International Center for Hadron Astrophysics, Chiba University, Chiba 263-8522, Japan

³⁵ Institute for Astrophysical Research, Boston University, 725 Commonwealth Avenue, Boston, MA 02215, USA

³⁶ Department of Astrophysics, St. Petersburg State University, Universitetsky pr. 28, Petrodvoretz, 198504 St. Petersburg, Russia

³⁷ Department of Physics and Astronomy and Space Science Center, University of New Hampshire, Durham, NH 03824, USA

³⁸ Physics Department and McDonnell Center for the Space Sciences, Washington University in St. Louis, St. Louis, MO 63130, USA

³⁹ Istituto Nazionale di Fisica Nucleare, Sezione di Napoli, Strada Comunale Cinthia, I-80126 Napoli, Italy

⁴⁰ Université de Strasbourg, CNRS, Observatoire Astronomique de Strasbourg, UMR 7550, F-67000 Strasbourg, France

⁴¹ Graduate School of Science, Division of Particle and Astrophysical Science, Nagoya University, Furo-cho, Chikusa-ku, Nagoya, Aichi 464-8602, Japan

⁴² Hiroshima Astrophysical Science Center, Hiroshima University, 1-3-1 Kagamiyama, Higashi-Hiroshima, Hiroshima 739-8526, Japan

⁴³ Department of Physics and Astronomy, Louisiana State University, Baton Rouge, LA 70803, USA

⁴⁴ Department of Physics, University of Hong Kong, Pokfulam, Hong Kong

⁴⁵ Department of Astronomy and Astrophysics, Pennsylvania State University, University Park, PA 16801, USA

⁴⁶ Université Grenoble Alpes, CNRS, IPAG, F-38000 Grenoble, France

⁴⁷ Center for Astrophysics, Harvard & Smithsonian, 60 Garden Street, Cambridge, MA 02138, USA⁴⁸ INAF Osservatorio Astronomico di Brera, via E. Bianchi 46, I-23807 Merate (LC), Italy⁴⁹ Dipartimento di Fisica e Astronomia, Università degli Studi di Padova, Via Marzolo 8, I-35131 Padova, Italy⁵⁰ Department of Astronomy, University of Maryland, College Park, MD 20742, USA⁵¹ Anton Pannekoek Institute for Astronomy & GRAPPA, University of Amsterdam, Science Park 904, 1098 XH Amsterdam, The Netherlands⁵² Guangxi Key Laboratory for Relativistic Astrophysics, School of Physical Science and Technology, Guangxi University, Nanning 530004, People's Republic of China*Received 2023 November 8; revised 2023 December 21; accepted 2023 December 22; published 2024 January 11*

Abstract

Cir X-1 is a neutron star X-ray binary characterized by strong variations in flux during its eccentric ~ 16.6 day orbit. There are also strong variations in the spectral state, and it has historically shown both atoll and Z state properties. We observed the source with the Imaging X-ray Polarimetry Explorer during two orbital segments, 6 days apart, for a total of 263 ks. We find an X-ray polarization degree in these segments of $1.6\% \pm 0.3\%$ and $1.4\% \pm 0.3\%$ at polarization angles of $37^\circ \pm 5^\circ$ and $-12^\circ \pm 7^\circ$, respectively. Thus, we observed a rotation of the polarization angle by $49^\circ \pm 8^\circ$ along the orbit. Because variations of accretion flow, and then of the hardness ratio, are expected during the orbit, we also studied the polarization binned in hardness ratio and found the polarization angle differing by $67^\circ \pm 11^\circ$ between the lowest and highest values of the hardness ratio. We discuss possible interpretations of this result that could indicate a possible misalignment between the symmetry axes of the accretion disk and the Comptonizing region caused by the misalignment of the neutron star's angular momentum with respect to the orbital one.

Unified Astronomy Thesaurus concepts: X-ray binary stars (1811); Polarimetry (1278); X-ray astronomy (1810); X-ray sources (1822)

1. Introduction

X-ray binaries (XRBs) consist of a compact object with a stellar companion orbiting it, from which it accretes matter. Flux and spectral variations in XRBs are thought to correspond to different accretion configurations. The spectrum of each state can be interpreted as a superposition of different components having a different relative flux: typically the accretion disk, emitting a soft, nearly thermal spectrum described by a blackbody or a multicolor disk, and a corona of hot plasma, whose electrons up-scatter the low-energy ambient photons, generating a hard X-ray component. In neutron star (NS) XRBs (NS-XRBs), the surface region, where the accreting matter is stopped, also contributes to the total emission. The interfacing region, which is coplanar to the accretion disk, is known as the boundary layer (BL; Shakura & Sunyaev 1988; Popham & Sunyaev 2001), while the gas layer at the NS surface, extending up to high latitudes, is known as the spreading layer (SL; Inogamov & Sunyaev 1999; Suleimanov & Poutanen 2006; Abolmasov et al. 2020). XRBs with a weakly magnetized NS are classified, according to their tracks on the hard/soft X-ray color diagram, as Z or atoll sources (Hasinger & van der Klis 1989; van der Klis 1989).

Cir X-1 is a weakly magnetized NS-XRB characterized by an eccentric ($e \sim 0.45$) ~ 16.5 day orbit (see, e.g., Kaluzienski et al. 1976; Schulz et al. 2020), during which its flux and spectrum change significantly, very different from any other known XRB. Cir X-1 has historically been shown to go through all the different states for both Z and atoll sources (Schulz et al. 2019). On the basis of its spectral characteristics, it was for a long time suspected to host a black hole, but the discovery of type I bursts undoubtedly proved that the compact

object is an NS (Tennant et al. 1986; Linares et al. 2010). During its orbit, the X-ray flux varies by 2 orders of magnitude, and there are also more irregular decades-long variations (D'Ai et al. 2012).

An extended emission from a supernova remnant has been found around Cir X-1 (Heinz et al. 2013) with an estimated age of 4600 yr, implying that the source is the youngest known XRB (as reported by Heinz et al. 2013). The young age is consistent both with the eccentricity of the orbit and with its irregular variations. Another characteristic that sets Cir X-1 apart from other XRBs is the presence of both radio and—X-ray jets, indicating the ejection of matter at relativistic speeds. The X-ray jets are clearly visible on both sides of the receding and approaching radio jet (Heinz et al. 2007; Soleri et al. 2009). Their presence, observed by Chandra either as a Doppler shift of emission lines or by directly imaging a diffuse and elongated emission, is interesting for comparing this system with black holes, showing that jets can be produced despite the shallower gravitational potential of NSs (Fender et al. 2004). The orientation of the radio jets has been reported to change with time either because of the precession of the regions from which they are emitted, where it is well accepted that they must be close to the compact object, or because of the interaction with the interstellar matter (Coriat et al. 2019).

Several models have been proposed to account for the peculiar orbital and state variations of Cir X-1. A dip in the light curve—followed by a flaring phase—is seen every orbit. This dip could be caused by a cold absorber; however, this would work only for high inclinations (D'Ai et al. 2012). According to Johnston et al. (1999), the eccentric orbit causes orbital variations in the mass accretion rate, producing the modulation in the X-ray luminosity. Schulz et al. (2019) suggested that the companion is a massive supergiant of Be type, which would imply that Cir X-1 is a high-mass Be XRB. The available observations until now have not been sufficient to discriminate among the different models.

⁵³ Deceased.

Table 1
Observational Data Used in This Paper, Reporting for Each Mission the Observation IDs, Live Time, and Start and End Times of Each Observation

Mission	ObsID	Live Time (s)	Start Time	End Time
IXPE	2002699	263,000	2023-08-02T11:24 2023-08-11T10:17	2023-08-04T23:52 2023-08-13T22:46
NICER	6689030104 6689030203	305 4325	2023-08-05T00:22 2023-08-13T00:27	2023-08-05T00:35 2023-08-13T20:57
NuSTAR	30902037002 30902037004	12,000 15,000	2023-08-04T21:51 2023-08-12T14:31	2023-08-05T09:01 2023-08-13T01:26

We report the first polarimetric study of Cir X-1 using the Imaging X-ray Polarimetry Explorer (IXPE), measuring the new observables of polarization degree (PD) and polarization angle (PA). With X-ray polarimetry we can discern, from different polarization signatures, the different emission mechanisms and the geometry of the regions closer to the compact object. In the absence of relativistic effects, the PA is expected to be either parallel or perpendicular to the main geometrical axis of the component; as a consequence, if two components (such as a disk and Comptonized region) are aligned, we expect their PAs to be either the same or orthogonal. If this is not the case, it can indicate that there is a geometrical misalignment between them, or that relativistic effects rotate the polarization plane (e.g., Connors & Stark 1977; Connors et al. 1980; Dovčiak et al. 2004; Loktev et al. 2020, 2022).

2. Observations

2.1. IXPE

IXPE (Soffitta et al. 2021; Weisskopf et al. 2022) is the first observatory combining detectors sensitive to X-ray polarization in the 2–8 keV energy band with X-ray optics. This mission, a collaboration between NASA and the Italian Space Agency, consists of three X-ray polarization sensitive gas pixel detectors (Costa et al. 2001; Bellazzini et al. 2006, 2007; Baldini et al. 2021) at the focus of three grazing incidence optics. Other than detecting polarization, IXPE simultaneously detects the energy, time of arrival, and celestial position of each X-ray detected.

IXPE observed Cir X-1 in two different pointings (2023-08-02T11:24 to 2023-08-04T23:52 and 2023-08-11T10:17 to 2023-08-13T22:46, joint in ObsID 02002699; see Table 1) to cover two different parts of the orbit for a net total exposure time of 263 ks. Neutron Star Interior Composition Explorer (NICER) and Nuclear Spectroscopic Telescope Array (NuSTAR) observations were performed to simultaneously partially cover the IXPE observation. IXPE data are reduced and corrected by the standard pipeline running at the Science Operations Center in NASA/MSFC and were downloaded from the IXPE public archive at HEASARC.⁵⁴ In the following analysis, event-by-event Stokes parameters are calculated following an unweighted approach (Kislat et al. 2015; Di Marco et al. 2022a) and computed using IXPEOBSSSIM 30.6.3 (Baldini et al. 2022); they are provided to the user in a reference frame projected on the sky. We selected the source in a circular region of radius 90'' centered on the source. Because of the high brightness of this source, the background is negligible (see Di Marco et al. 2023a).

The top panel of Figure 1 shows the IXPE light curve during these observations overlaid with data from the Monitor of All-

sky X-ray Image (MAXI; Matsuoka et al. 2009) telescope. MAXI is mounted on board the International Space Station and monitors X-ray sources continuously; therefore, its light curve allows one to study the flux variations in Cir X-1 over its entire orbit, even outside the IXPE observation.

To verify possible changes in the accretion flow of Cir X-1, we study its flux and hardness ratio (HR) variations over the IXPE observing time. The bottom panel of Figure 1 shows the IXPE HR, defined as

$$HR_{IXPE} = \frac{\text{Counts [4–8 keV]}}{\text{Counts [3–4 keV]}}. \quad (1)$$

The same plots show a division of the overall observations in three phase intervals, which we will use in the following to study the polarization along the orbit of Cir X-1: P1 (phase from 0.21 to 0.22), P2 (phase from 0.22 to 0.36), and P3 (phase from 0.75 to 0.90). We clearly see during the first observation a transition from a low-flux hard state to a high-flux soft state. The IXPE observation starts just when the source is coming out from the dip, as shown by the MAXI light curve, so that the low–hard state corresponds to this part of the orbit.

Figure 2 (left) shows the hardness–intensity diagram for the three phase intervals obtained from the IXPE data. We clearly see a variation in hardness–intensity between the low–hard and high–soft states when moving from the first to the second phase interval. We also see that the HR is, on average, slightly larger in the third phase interval, when the flux is lower, compared to the second phase interval. The same effect is also seen in the color–color diagram (right panel of Figure 2), which shows the evolution of the source in two colors defined for the low- and high-energy bands.

Tominaga et al. (2023) studied Cir X-1 for an extended period and divided (Figure 2 of their paper) the orbit into different phases: a dip phase, where the X-ray flux is low due to strong absorption and whose end corresponds to P1 in this paper; a flaring phase, with rapid changes, corresponding to P2 in this paper; and a stable phase, with a gradual decrease in X-ray flux, corresponding to P3 in this paper.

2.2. NICER

NICER (Gendreau et al. 2016), mounted on board the International Space Station, observed Cir X-1 during part of the IXPE observations. ObsIDs 6689030104 (right at the end of the first IXPE observation) and 6689030203 (during the second IXPE observation; see Table 1) were used to study the spectral components of Cir X-1 (see Section 3). NICER consists of 56 coaligned concentrator X-ray optics, each with a silicon drift detector at its focus, and, although it does not have imaging capabilities, it has a large collecting area in the energy interval of 0.2–12 keV. These observations were obtained in the

⁵⁴ <https://heasarc.gsfc.nasa.gov/docs/ixpe/archive/>

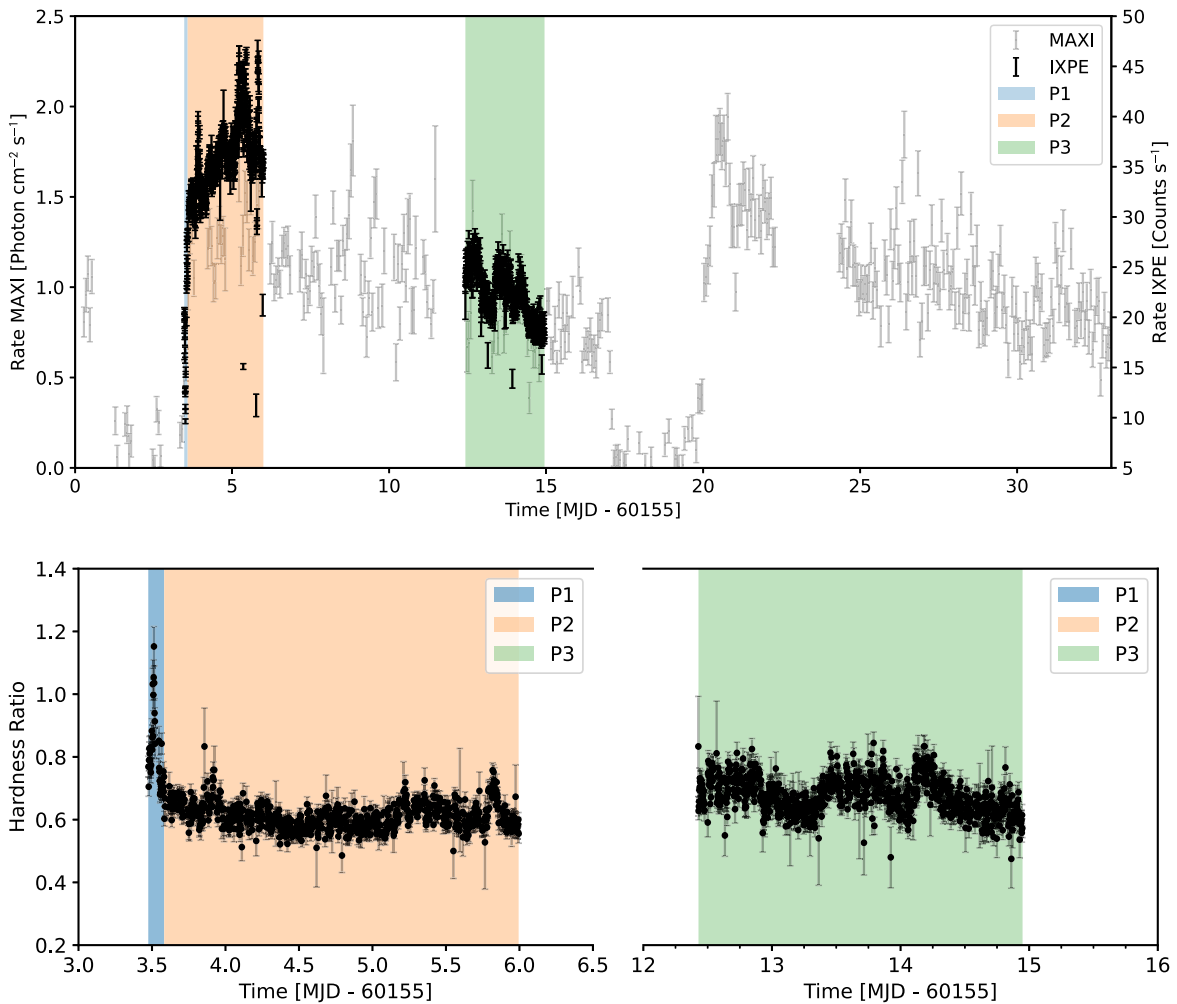


Figure 1. Evolution of the X-ray properties of Cir X-1. (Top) Rate obtained by MAXI (2–20 keV) and IXPE over two orbits binned in 180 s time bins. (Bottom) HR obtained from IXPE (Equation (1)) during the observations binned in 500 s time bins. There is a clear change in state from the hard to the soft at the beginning of the IXPE observation; based on this, we divide the analysis into the three phase intervals indicated in the plots by the colored regions.

framework of GO Cycle 5 (proposal 6189); data were processed with the NICER Data Analysis Software v010a released on 2022 December 16 provided under HEASOFT v 6.31.1 with the CALDB version released on 2022 October 30.

2.3. *NuSTAR*

NuSTAR (Harrison et al. 2013) consists of two focal plane modules (FPMA and FPMB) providing broadband X-ray imaging, spectroscopy, and timing in the energy range of 3–79 keV with an angular resolution of 18'' (FWHM) and spectral resolution of 400 eV (FWHM) at 10 keV, and it is the only observatory employing multilayer X-ray optics capable of focusing hard X-rays. We used the Cir X-1 observations at the end of the first IXPE observation (ObsID 30902037002) and during the second one (ObsID 30902037004; see Table 1), performed in the framework of GO Cycle 9 (proposal 9212).

NuSTAR data were processed using the standard Data Analysis Software (NUSTARDAS v2.1.2 from 2022 February 12) provided under HEASOFT v 6.31.1 with the CALDB version released on 2023 April 4. The source was selected from a circular 150'' radius region centered on the source position; the background was extracted in a similar region but in a position of the field of view out of the source.

3. Spectroscopic Analysis

Aiming to constrain the spectral model and understand the different components, we analyzed NICER (in 1–10 keV) and *NuSTAR* (in 3–25 keV) data; the ObsIDs are those reported above and were selected to overlap and have a short duration, so that there would be no HR variations. Previous spectral fits, such as in the broadband BeppoSAX spectra (Iaria et al. 2002, 2005), reported the presence of two components: a blackbody disk and a Comptonization component. However, the temperature of one of the components—the disk—has been reported to be low (~ 0.5 keV; Iaria et al. 2008), so the disk is not expected to contribute significantly to the IXPE energy band.

We attempted to fit the continuum with the two components reported in the literature: *diskbb* (Mitsuda et al. 1984; Makishima et al. 1986), associated with the disk or NS surface, and *comptt* (Titarchuk 1994), associated with the Comptonization in the BL/SL. We saw an excess in the residuals around 6 keV, associated with a broad iron line due to reflection from the disk, and around 1.7 keV, associated with a silicon line, suspected to be an instrumental NICER feature due to an incorrect calibration of the response, which becomes visible at the high flux observed from Cir X-1. To estimate the absorption from the interstellar medium, we set the abundances

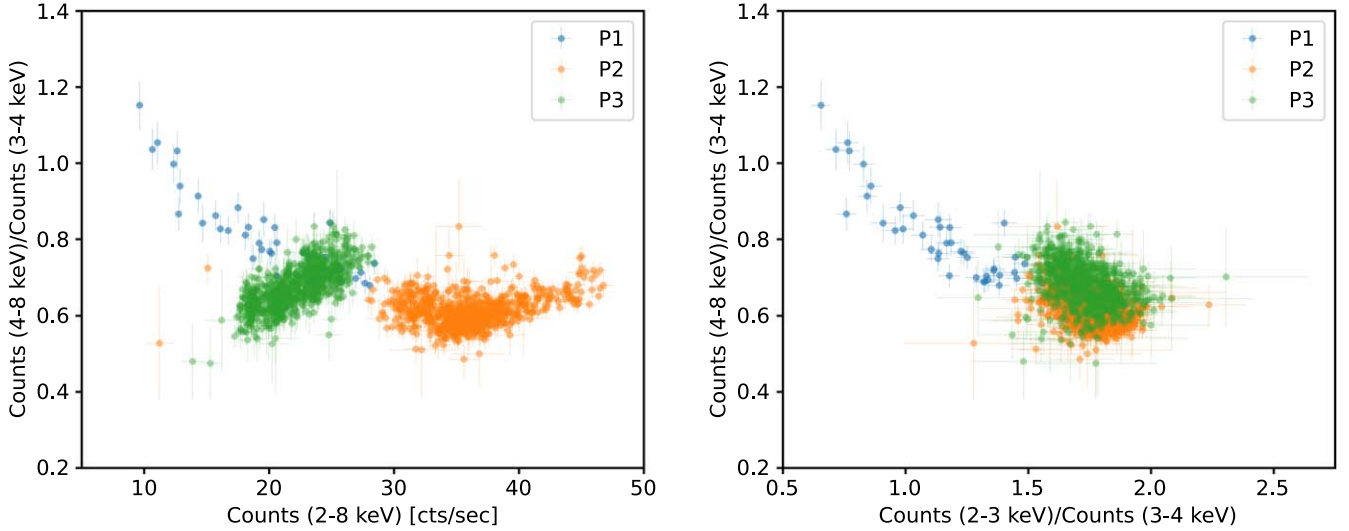


Figure 2. Hardness–intensity (left) and color–color (right) diagrams during the IXPE observations, binned in time bins of 180 s, with color highlighting the three phase intervals chosen for the subsequent analysis.

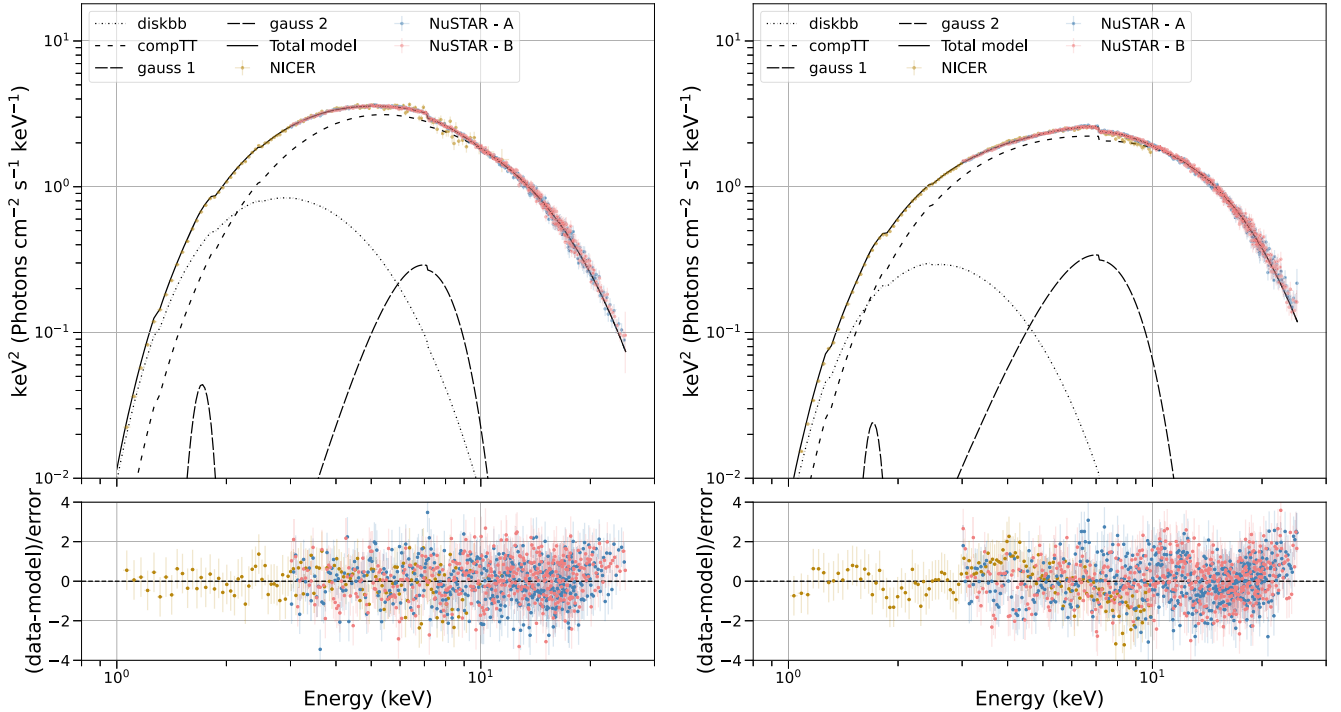


Figure 3. Spectral energy distribution of Cir X-1 during P2 (left) and P3 (right) in EF_E representation using NICER and NuSTAR (FPMA and FPMB) data and showing the different model components.

at the *wilm* values (Wilms et al. 2000); we started with a *tbabs* model but found that there were residuals better taken into account using *tbfeo*. The resulting model is written in XSPEC as *tbfeo*(diskbb+comptt+Gauss+Gauss)*.

We started by leaving all the parameters free but found the temperature of the disk to be degenerate with its norm. We then fixed the disk temperature to a value minimizing the χ^2 and left the norm free in the subsequent fit; the resulting best-fit models are shown in Figure 3, and the parameters are given in Table 2. We see that the flux during P3 is lower than in P2, and the spectrum is harder. This is also reflected in a significantly higher optical depth τ_p during P3, while the electron temperature is nearly the same. We left a free constant between

NICER and NuSTAR, as well as between the different NuSTAR modules: the two NuSTAR modules, normalized to NICER, have values of 1.16 and 1.14 in P2 and 1.39 and 1.37 in P3. Since NuSTAR shows calibration uncertainties (Madsen et al. 2022), we left free a gain offset in the fit. No systematic errors were added to the fits (a known systematic error of $<1.5\%$ is already applied to NICER data by the NICER pipeline *nicerl3-spect*). From the relative fluxes of the components in the nominal IXPE energy band of 2–8 keV, we see that, even if both components are present, the dominant component is *comptt*. One of the Gaussians is an instrumental NICER feature, while the other is not visible due to a low IXPE energy resolution with respect to NICER and

Table 2
Best-fit Parameters of the Spectral Model `tbfeo*(diskbb+comptt+Gauss+Gauss)` Applied to the Simultaneous Data from NICER and NuSTAR

Model	Parameter	P2	P3
tbfeo	N_{H} (10^{22} cm $^{-2}$)	$3.0^{+0.5}_{-0.8}$	$3.09^{+0.01}_{-0.31}$
	Fe (10^{22} cm $^{-2}$)	<1.6	<0.3
	O (10^{22} cm $^{-2}$)	$2.6^{+1.1}_{-0.6}$	$2.7^{+0.2}_{-0.3}$
diskbb	kT_{in} (keV)	0.85 ^a	0.7 ^a
	norm ($[R_{\text{in}}/D_{10}]^2 \cos \theta$)	417^{+32}_{-35}	360^{+12}_{-2}
comptt	kT_0 (keV)	1.00 ± 0.03	0.74 ± 0.01
	kT_c (keV)	$2.56^{+0.03}_{-0.02}$	$2.539^{+0.006}_{-0.003}$
	τ	$4.93^{+0.09}_{-0.12}$	$7.22^{+0.08}_{-0.02}$
	norm	0.68 ± 0.02	$0.50^{+0.01}_{-0.05}$
Gauss	E_{line} (keV)	6.5 ± 0.1	$6.04^{+0.01}_{-0.22}$
	σ (keV)	$1.27^{+0.07}_{-0.08}$	$1.75^{+0.01}_{-0.05}$
	norm (photon s $^{-1}$ cm $^{-2}$)	0.017 ± 0.003	0.034 ± 0.002
Gauss	E_{line} (keV)	1.7 ^a	1.7 ^a
	σ (keV)	0.08 ± 0.03	0.08 ^a
	norm (photon s $^{-1}$ cm $^{-2}$)	0.009 ± 0.0003	0.005 ± 0.001
χ^2/dof		1271/1222 = 1.04	1398/ 1226 = 1.14
Photon flux in 2–8 keV			
F_{tot} (10^{-8} erg s $^{-1}$ cm $^{-2}$)		2.09	1.53
$F_{\text{diskbb}}/F_{\text{tot}}$		0.18	0.09
$F_{\text{comptt}}/F_{\text{tot}}$		0.79	0.85
$F_{\text{gauss}}/F_{\text{tot}}$		0.03	0.06

Notes. Errors are reported at a 68% CL.

^a Frozen.

NuSTAR. Therefore, in the following spectropolarimetric analysis of the IXPE data, we only considered the `comptt` component.

4. Polarization Analysis

We studied the polarization of Cir X-1 in the three different phase and HR intervals. We first performed a study independent of any spectral model using the `pcube` algorithm of the IXPEOBSSSIM software (Baldini et al. 2022). Then we also studied the polarization applying the spectropolarimetric analysis in XSPEC (Arnaud 1996) by fitting the I , Q , and U spectra. In agreement with the spectral models reported in literature (see, e.g., D’Ài et al. 2012), we describe the I spectrum with the model: `tbabs*comptt`, setting the abundances to the values of Wilms et al. 2000, for the `comptt` model the geometry assumed is a disk (Titarchuk 1994), the hydrogen column density is fixed at the values found in the fit from the previous section for P2 and P3, and for the intermediate value for the HR bins. We did not fit the P1 data, since they are too short, have too few counts for polarimetric studies, and have no contemporaneous NuSTAR data (however, we still studied these data using `pcube`). To take into account IXPE calibration uncertainties (Di Marco et al. 2022b; Rankin et al. 2023), we left the gain slope and offset free, obtaining values, respectively, of the order of 95% for the slope and in the 0.005–0.2 keV range for the offset.

The results for the spectral modeling in the two phase intervals and three HR intervals are reported in Table 3. For the spectropolarimetric analysis, we use the best-fit spectral fits from Table 3 and then fit Q and U using the model `polconst` in XSPEC (see Table 4 for the obtained results). We also attempted fitting with the `pollin` model, but this gave no improvement over `polconst`. We considered fitting with a double `polconst` model (`tbabs*(comptt*polconst + diskbb*polconst)`). However, in this case, due to the low flux of `diskbb`, not all bins under consideration provide an acceptable fit with all parameters constrained, and we are not able to separate the two components.

4.1. Polarization along the Orbital Phase Intervals

We first studied the PD and PA into each single phase interval in the whole IXPE 2–8 keV energy band. Figure 4 (top) shows a polar plot representing the PD and PA confidence regions in the three phase intervals defined in Figure 1. The polarization in the first phase interval (P1)—the low–hard state—is unconstrained, as expected due to the low counts; the polarization in the remaining two phase intervals—P2 and P3—is significantly detected at a confidence level (CL) higher than 99%. We also observe a clear rotation of the PA by $49^\circ \pm 8^\circ$ between P2 and P3; a 90° rotation is not consistent with this result at a 99.5% CL. The numerical values of polarization obtained in this analysis are reported in Table 5. The results obtained in these phase intervals using XSPEC are summarized in Table 4.

We also attempted to measure the polarization properties in different energy bands (bottom panels of Figure 4). No evidence for an energy dependence at a 90% CL is observed in any energy band; however, there are low-significance hints of a PD energy dependence in P2 and P3. There is also a low-significance indication of a PA rotation with energy in P1; the PA at lower energies is consistent with the PA measured in P3, while at higher energies, it is similar to that of P2.

4.2. Polarization as a Function of HR

Since HR varies during the orbit—even inside the phase intervals we considered above—we studied the polarization in different HR states. This analysis is also useful to have an idea, given the difficulties in the determination of the spectral components, of the polarization of the different emission regions/components. We used the HR values in the time bins of Figure 1 (bottom) to define three different HR intervals: HR1 in the range 0.5–0.6, HR2 in the range 0.6–0.7, and HR3 in the range 0.7–0.8. Given the large uncertainty on each HR value—at a level of ~ 0.05 —we used the average HR in larger time bins of 2000 s each to populate the three HR intervals in the polarimetric analysis. This average curve is reported in Figure 5 (top).

The polarization computed from events in these HR bins is shown in Figure 5; the numerical values are reported in Table 5, while those obtained with XSPEC are in Table 4. The two estimates are compatible. In the 2–8 keV energy band, the PD is compatible in the three HR intervals, while the PA shows a gradual rotation as the HR changes, with a total rotation of the PA by $67^\circ \pm 11^\circ$ between the lowest and highest HR bins; a 90° rotation is not consistent with this result at a 68.2% CL.

Table 3
Best-fit Parameters Obtained by Fitting IXPE Data with the XSPEC Model `const*tbabs*comptt`

	χ^2/dof	N_{H} (10^{22} cm^{-2}) (fixed)	T_0 (keV)	kT_e (keV)	τ_p	Norm
P2	417/435	2.77	$0.50^{+0.02}_{-0.04}$	$1.57^{+0.03}_{-0.04}$	11.5 ± 0.4	$1.71^{+0.05}_{-0.04}$
P3	446/435	2.65	$0.59^{+0.04}_{-0.03}$	$2.15^{+0.11}_{-0.09}$	9.4 ± 0.4	$0.77^{+0.03}_{-0.04}$
HR1	404/429	2.7	$0.62^{+0.02}_{-0.08}$	$1.72^{+0.07}_{-0.16}$	$9.1^{+1.4}_{-0.4}$	$1.5^{+0.2}_{-0.1}$
HR2	397/435	2.7	$0.50^{+0.01}_{-0.02}$	$1.68^{+0.02}_{-0.03}$	$11.4^{+0.3}_{-0.1}$	$1.21^{+0.02}_{-0.01}$
HR3	398/433	2.7	$0.61^{+0.03}_{-0.05}$	$2.1^{+0.2}_{-0.1}$	$10.1^{+0.9}_{-0.5}$	$0.88^{+0.02}_{-0.04}$

Note. Uncertainties are at a 68% CL.

Table 4
Polarization Properties Obtained by Fitting the XSPEC Model `const*tbabs*polconst*comptt` to the IXPE I , Q , and U Data

	χ^2/dof	PD (%)	PA (deg)
P2	594/589	1.3 ± 0.2	40 ± 5
P3	603/589	1.1 ± 0.3	-10 ± 7
HR1	609/583	1.1 ± 0.3	43 ± 9
HR2	551/589	1.1 ± 0.2	27 ± 6
HR3	549/587	1.6 ± 0.4	-24 ± 7

Note. Uncertainties are at a 68% CL.

The polarization in different energy bands is reported in Figure 5 (bottom). No evidence for an energy trend at a 90% CL is observed in any energy band, but there are only hints of an increase of PD with energy.

5. Discussion and Conclusions

We studied the X-ray polarization of the NS-XRB Cir X-1 for the first time. With the available statistics, there is no significant variation with energy (see bottom panels of Figures 4 and 5). In other XRBs observed by IXPE, an increase of the PD with energy was observed, but in this case, we only have hints of such an increase; we also find low-significance hints of a rotation of the PA with energy in the hard state at the beginning of the IXPE observation (P1 of Figure 4), which is the state where the Comptonization component is stronger. Comparing with Gnarini et al. (2022) and Poutanen et al. (2023), we find that the energy trend in polarization for the Cir X-1 observation is compatible with a shell or sandwich/wedge coronal geometry (with an inclination of $<80^\circ$) but not a slab geometry, for which a pronounced increase with energy would be expected. However, none of these two scenarios can fully explain our observation, where a change of the polarization is observed as a function of time and HR. This can be explained in terms of a scenario such as the one in Figure 6 (described in more detail below), where an SL and a BL are present, allowing for a deeper analysis capable of estimating the system inclination and the inclination of the NS axis with respect to the disk, but no such model is currently available in the literature.

Along Cir X-1's orbit, we observe a rotation of the PA by $49^\circ \pm 8^\circ$ between different phase intervals (Figure 4), while the PD stays constant within the same observing phase intervals. With the accretion flow expected to be related to the orbital variations of Cir X-1, we perform an analogous study in HR intervals; we also observe in this case a constant PD with a rotation of the PA by $67^\circ \pm 11^\circ$ (Figure 5). The rotation

between phase intervals is compatible with the rotation between HRs within a 68% CL.

From a spectral point of view, `comptt` dominates in the IXPE energy band. However, at least two components are present, as reported in Section 3. Thus, the variations along the orbit can be due to a superimposition of two different components contributing in a different way along the phase intervals. Looking at the top panel of Figure 5, we see that all phase intervals are dominated by HR2 ($\sim 60\%$), with a contribution from HR1 ($\sim 35\%$) in P2 and from HR3 ($\sim 35\%$) in P3. This confirms a scenario where the accretion flow—and the HR—varies along the orbit, with the harder state gradually becoming dominant as we get further away from the end of the dip (close to the beginning of the first IXPE observation). This is compatible with a model in which the accretion disk changes during the orbit due to its eccentricity (Johnston et al. 1999). In this model, the modulation in the X-ray luminosity is due to orbital variations in the mass accretion of the compact star; during the periastron passage, the companion star overfills its Roche lobe, and the accretion disk is perturbed through both tidal interaction and a sudden surge of material inflow, triggering an X-ray outburst.

We can interpret variations of the PA as due to two spectral components with significantly different PAs: a lower-energy one dominating at low HR and a harder one dominating at higher HR. In the intermediate HRs, the two components are mixed. Such a two-component model, composed of, e.g., a multicolor blackbody from the accretion disk and a Comptonized component, is the obvious candidate to explain two components in the polarization and so has been proposed for the other IXPE observations of weakly magnetized accreting NSs (Ursini et al. 2023a; Di Marco et al. 2023b; Capitanio et al. 2023; Cocchi et al. 2023; Farinelli et al. 2023). From simple geometrical considerations, and in the absence of relativistic effects, each component can be expected to be polarized either parallel or orthogonal to its symmetry axis. The PA of the optically thick accretion disk is expected to be perpendicular to the position angle of the rotation axis. Relativistic effects may cause a small decrease (for counterclockwise rotation) of the PA by 5° – 10° (Loktev et al. 2022). The Comptonization component can be associated either with the BL (which is coplanar with the accretion disk) or with the SL at the NS surface. The PA of the BL is likely nearly aligned with the PA of the accretion disk. In the absence of relativistic effects, the PA of the optically thick SL emission is parallel to the rotation axis. Due to aberration and Doppler boosting, the emission is expected to be dominated by the part of the SL moving toward the observer, breaking the symmetry and causing a decrease (also for counterclockwise rotation) of the PA by up to $\sim 20^\circ$ – 30° depending on the parameters (A. Bobrikova et al. 2023, in

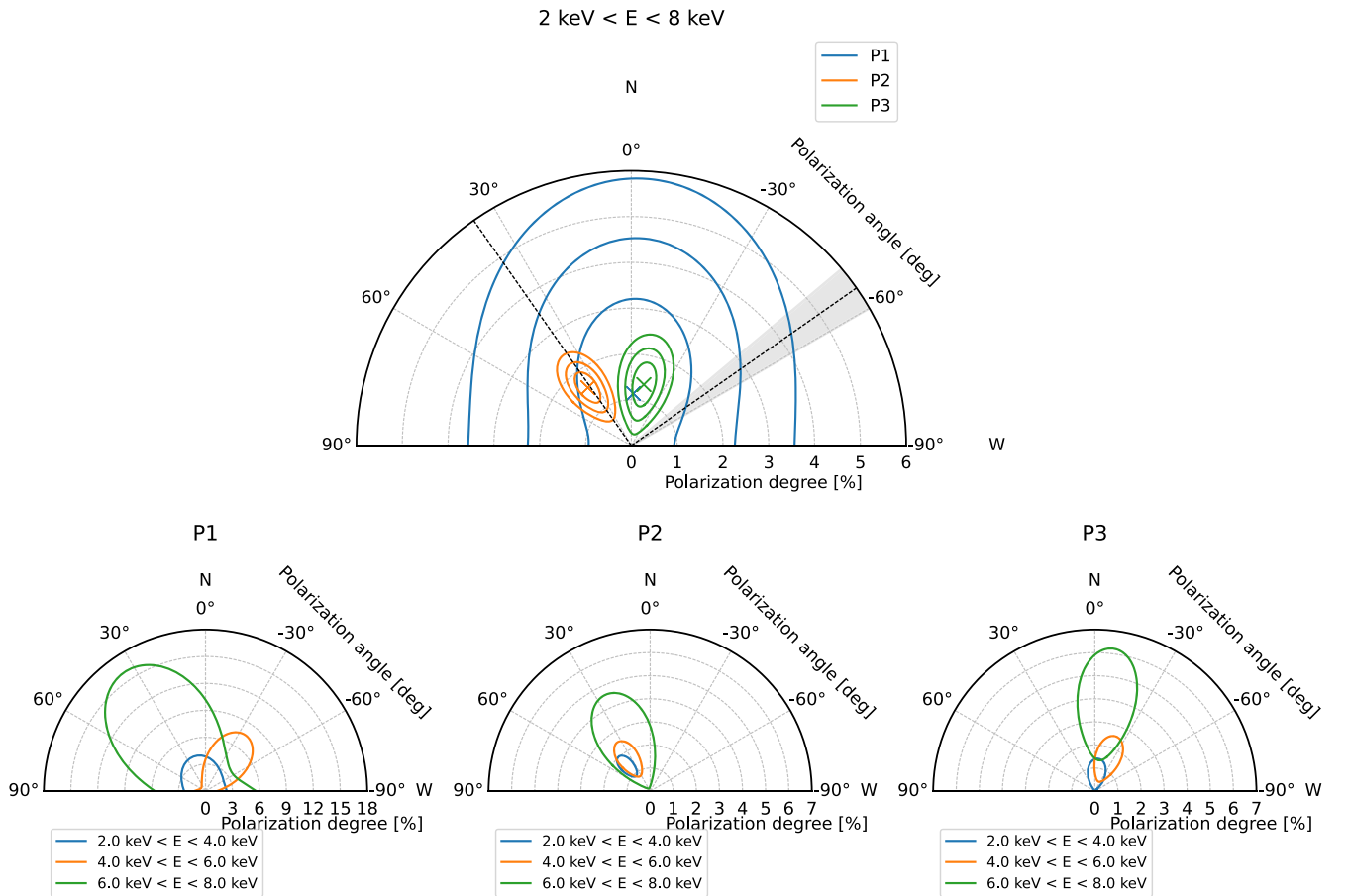


Figure 4. Polar plot of polarization, computed using the `pcube` algorithm from the `IXPEOBSSIM` software (Baldini et al. 2022), for the three phase intervals defined in Figure 1. (Top) Polarization in the entire IXPE energy band is reported. The shaded region indicates the direction of the jet (see discussion), and the black lines indicate this direction and its orthogonal direction. Contours are reported at the 68%, 95%, and 99% CLs. (Bottom) Polarization in different energy bands for the three phase intervals, with contours showing the 90% CL.

Table 5

Polarization for Different Phase Intervals and HR Using `pcube`

	PD (%)	PA (deg)	Q/I (%)	U/I (%)	MDP (%)
P1	1.1 ± 1.4	-2 ± 34	1.1 ± 1.4	-0.1 ± 1.4	4.1
P2	1.6 ± 0.3	37 ± 5	0.4 ± 0.3	1.5 ± 0.3	0.79
P3	1.4 ± 0.3	-12 ± 7	1.2 ± 0.3	-0.5 ± 0.3	0.98
HR1	1.6 ± 0.4	40 ± 7	0.2 ± 0.4	1.5 ± 0.4	1.2
HR2	1.3 ± 0.3	24 ± 6	0.9 ± 0.3	1.0 ± 0.3	0.79
HR3	1.9 ± 0.5	-26 ± 7	1.2 ± 0.5	-1.5 ± 0.5	1.5

Note. Uncertainties are at a 68% CL. The minimum detectable polarization (MDP) is the maximum polarization produced by statistical fluctuations at a 99% CL.

preparation). If the SL is optically thin, the PA may rotate by an additional 90° (Sunyaev & Titarchuk 1985; Viironen & Poutanen 2004). However, it is clear from this consideration that the difference in the PA of 50° – 60° , as found for Cir X-1, is impossible to produce.

The coexistence of two components with such a large difference in the PA may be explained if their symmetry axes are not aligned. This can be related, for example, to a misalignment of the NS angular momentum with respect to the orbital axis, thus causing a shift of the symmetry axis of the Comptonization region (associated with the SL) with respect to the disk (Abolmasov et al. 2020). We note here that Cir X-1 is

not the only source for which such a misalignment might be present, but there are other hints; in Cyg X-2, the PAs of the two components are 66° apart (see Figure 7 in Farinelli et al. 2023), while in XTE J1701–462 and GX 5–1, the difference is $\sim 40^\circ$ (Cocchi et al. 2023; Fabiani et al. 2023). Also, X-ray polarimetry provided evidence for a misalignment in the X-ray pulsar Her X-1 (Doroshenko et al. 2022). Such a misalignment is in fact more likely for Cir X-1 than for other NS systems, as the system is younger than 4600 yr (Heinz et al. 2013); if the newly formed NS spins out of plane with respect to the binary system, there is not enough time to come to the alignment of the spinning axes.

At the same time, the accretion disk itself has a lower temperature compared to the Comptonization components (Iaria et al. 2008) and does not contribute significantly to the IXPE band. Thus, the only other option for the second component is the BL. At low accretion rates (Figure 6, left), the disk is terminated at the innermost stable orbit of ~ 3 Schwarzschild radii (i.e., about 13.5 km for a $1.5 M_\odot$ NS), which is likely larger than the NS radius of ~ 12 km (e.g., Näätäla et al. 2017; Annala et al. 2022). In this situation, the BL does not exist at all, and matter freefalls on the NS surface, forming an SL. Thus, the PA would correspond to the orientation of the NS rotation axis on the sky. At high accretion rates (Figure 6, right), the thickness of the SL grows, connecting it to the accretion disk through the BL. In this case, the PA would be related to the symmetry axis of the disk.

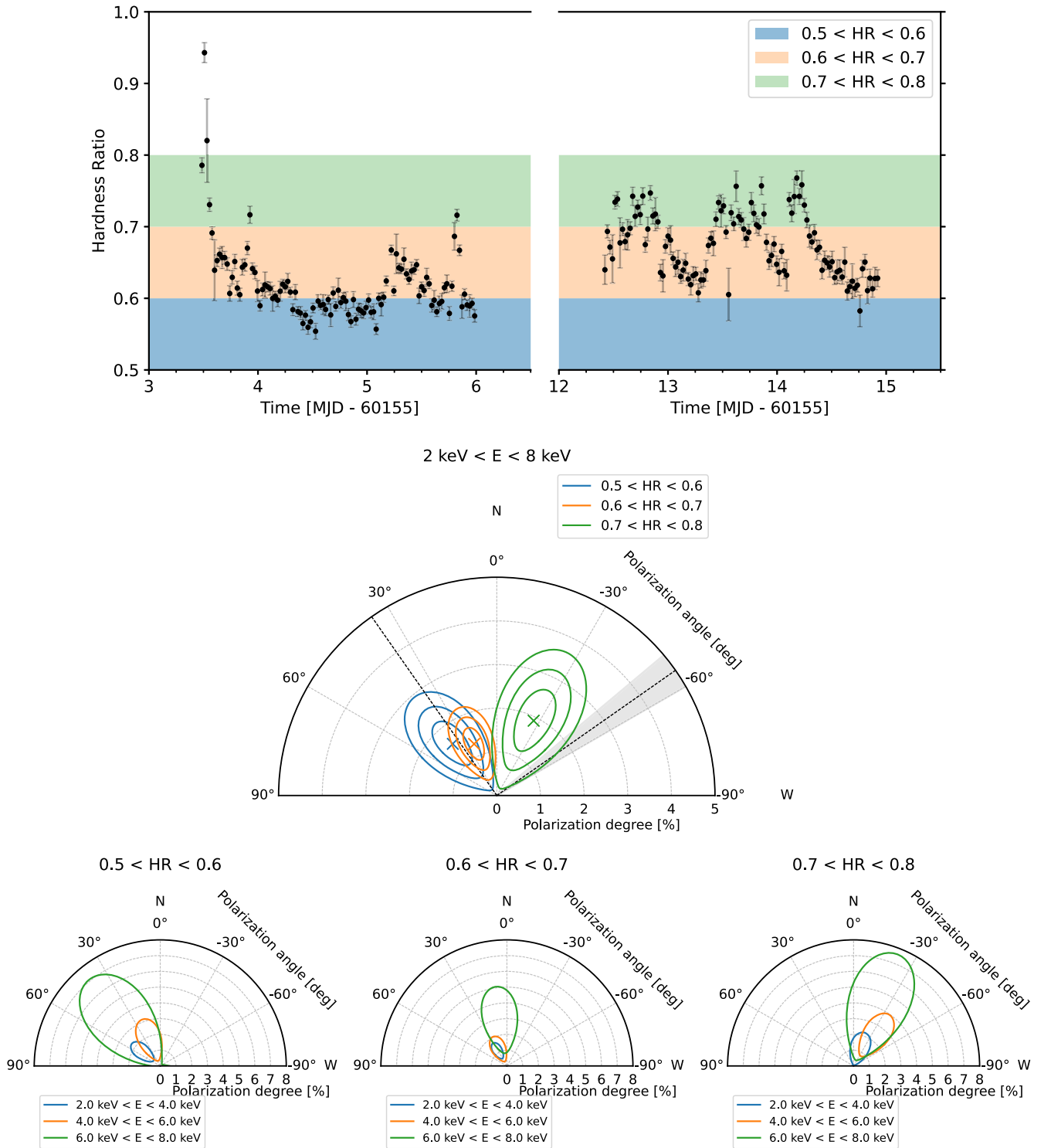


Figure 5. Study of polarization binned in HR. (Top) HR trend with time (2000 s time binning); the colored bands identify the chosen binning for HR. (Middle) Polar plot of polarization, computed using the model-independent `pcube` algorithm from the IXPEOBSSIM software (Baldini et al. 2022), for events in different intervals of HR reported in the top panel in the energy band 2–8 keV, where the shaded region indicates the direction of the jet (see discussion), and the black lines indicate this direction and its orthogonal direction. Contours are reported at 68%, 95%, and 99% CLs. (Bottom) Polarization in different energy bands. Contours are reported at a 90% CL.

Tominaga et al. (2023) modeled Cir X-1 as an accretion disk covered by a partially covering medium and interpreted the different phases of the orbit as changes in these two components. Their observations cover the dip for much longer than the IXPE polarimetric ones, where there is no significant

polarimetric information for this phase; if we had observed the dip for longer with IXPE, we might have expected a high PD due to obscuration, as observed in black hole systems (Ursini et al. 2023b; Veledina et al. 2023). It is interesting to note how their model is very good at predicting observational features

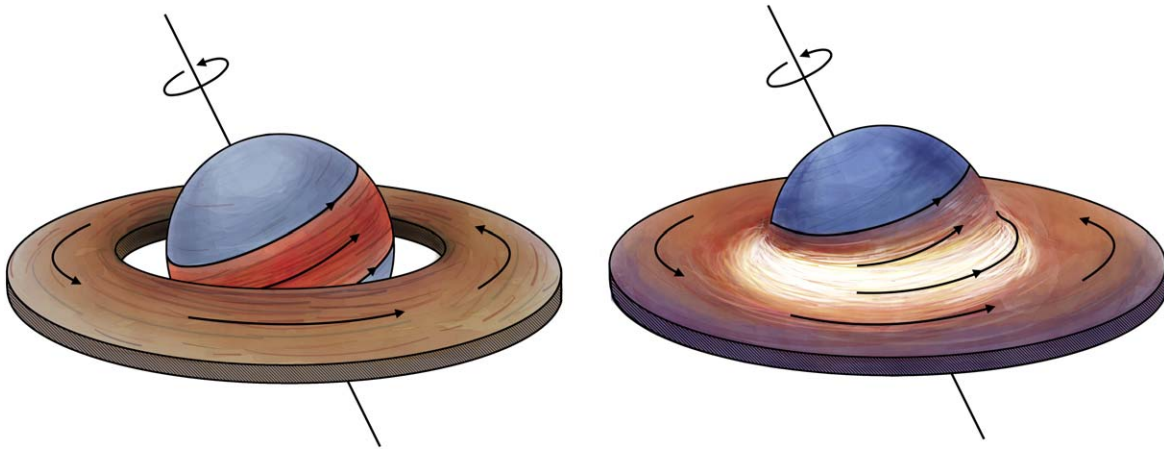


Figure 6. Illustration of a possible accretion geometry in Cir X-1. (Left) Low accretion rate case, when there is a gap between the disk and the NS surface, and the full SL is developed. (Right) High accretion rate case, where the disk touches the NS surface, and the BL is emitting (with a PA almost perpendicular to the symmetry axis of the disk).

such as lines, while to interpret the polarization, we need a geometric model dealing with different features, such as the model we outlined in this paper.

In order to understand the geometry of the inner accretion flow in Cir X-1, it is now worth relating the observed PAs to the orientation of the jet. Cir X-1 is among the few NS-XRBs showing jets in both the radio and the X-ray. The position angle of the (approaching) jet measured in the radio lies in the range 110° – 140° (Fender et al. 1998; Tudose et al. 2008; Sell et al. 2010; Calvelo et al. 2012; Miller-Jones et al. 2012). Also in the X-ray, the signature of the (receding) jet is found in the northwest direction at position angles of about -70° and -35° (Heinz et al. 2007; Soleri et al. 2009), while the approaching jet is seen in the PA interval of 90° – 150° (Soleri et al. 2009). Thus, the average jet direction seems to be nearly orthogonal to the direction of the X-ray polarization in P2 (and at H1 and H2; see Table 5), which we associate with the BL emission. On the other hand, the X-ray polarization at the highest HR (HR3) is $\sim 1.3\sigma$ apart from the jet direction (-35° or 140° – 150°). Finally, the X-ray PA of -12° during P3 is clearly neither parallel nor perpendicular to the jet. Associating the observed PA with the SL implies a misalignment of the NS’s angular momentum from the orbital axis by about 30° (Figure 6). Because the PA in this case is larger than the jet position angle, the rotation of the SL (and the disk) has to be clockwise, corresponding to an inclination exceeding 90° .

Although a large spread in the position angles measured for the jet can be explained by precession (Sell et al. 2010; Calvelo et al. 2012), such an interpretation does not work for the variations of the X-ray PAs because of the much shorter timescales involved and the detection of different PAs at different HRs. This gives further support to the interpretation that variations of the PA are caused by different spectral components (accretion disk, BL, and SL) dominating at different times. With the data at hand, it is impossible to extract those components from the spectra; variations of the PA, however, strongly support the idea that the NS angular momentum is misaligned from the orbital one, which is a necessary requirement for the precession to operate. The X-ray polarimetric data thus provide a unique view of the geometry of the accreting NS Cir X-1.

Acknowledgments

The Imaging X-ray Polarimetry Explorer (IXPE) is a joint US and Italian mission. The US contribution is supported by the National Aeronautics and Space Administration (NASA) and led and managed by its Marshall Space Flight Center (MSFC), with industry partner Ball Aerospace (contract NNM15AA18C). The Italian contribution is supported by the Italian Space Agency (Agenzia Spaziale Italiana, ASI) through contract ASI-OHBI-2022-13-I.0, agreements ASI-INAF-2022-19-HH.0 and ASI-INFN-2017.13-H0, and its Space Science Data Center (SSDC) with agreements ASI-INAF-2022-14-HH.0 and ASI-INFN 2021-43-HH.0, as well as by the Istituto Nazionale di Astrofisica (INAF) and the Istituto Nazionale di Fisica Nucleare (INFN) in Italy. This research used data products provided by the IXPE Team (MSFC, SSDC, INAF, and INFN) and distributed with additional software tools by the High-Energy Astrophysics Science Archive Research Center (HEASARC) at NASA Goddard Space Flight Center (GSFC). This research has made use of the MAXI data provided by RIKEN, JAXA, and the MAXI team.

We acknowledge support from Academy of Finland grants 333112, 355672, and 349144 (J.P., A.V., S.S.T.) and the German Academic Exchange Service (DAAD) travel grant 57525212 (V.D.). V.Kr. acknowledges support from the Finnish Cultural Foundation. F.A. and A.P. acknowledge financial support from the INAF Research Grant “Uncovering the optical beat of the fastest magnetized neutron stars (FANS)” and the Italian Ministry of University and Research (MUR), PRIN 2020 (prot. 2020BRP57Z), “Gravitational and Electromagnetic-wave Sources in the Universe with current and next-generation detectors (GEMS).” I.L. was supported by the NASA postdoctoral program at the Marshall Space Flight Center, administered by Oak Ridge Associated Universities under contract with NASA. F.X. is supported by the National Key R&D Program of China (grant No. 2023YFE0117200) and by the National Natural Science Foundation of China (grant No. 12373041).

Facilities: IXPE, NICER, NuSTAR, MAXI.

Software: IXPEOBSSIM (Baldini et al. 2022), XSPEC (Arnaud 1996), HEASOFT (Nasa Heasarc 2014).

ORCID iDs

John Rankin  <https://orcid.org/0000-0002-9774-0560>
 Fabio La Monaca  <https://orcid.org/0000-0001-8916-4156>
 Alessandro Di Marco  <https://orcid.org/0000-0003-0331-3259>
 Juri Poutanen  <https://orcid.org/0000-0002-0983-0049>
 Anna Bobrikova  <https://orcid.org/0009-0009-3183-9742>
 Vadim Kravtsov  <https://orcid.org/0000-0002-7502-3173>
 Fabio Muleri  <https://orcid.org/0000-0003-3331-3794>
 Maura Pilia  <https://orcid.org/0000-0001-7397-8091>
 Alexandra Veledina  <https://orcid.org/0000-0002-5767-7253>
 Rob Fender  <https://orcid.org/0000-0002-5654-2744>
 Philip Kaaret  <https://orcid.org/0000-0002-3638-0637>
 Dawoon E. Kim  <https://orcid.org/0000-0001-5717-3736>
 Andrea Marinucci  <https://orcid.org/0000-0002-2055-4946>
 Herman L. Marshall  <https://orcid.org/0000-0002-6492-1293>
 Alessandro Papitto  <https://orcid.org/0000-0001-6289-7413>
 Allyn F. Tennant  <https://orcid.org/0000-0002-9443-6774>
 Sergey S. Tsygankov  <https://orcid.org/0000-0002-9679-0793>
 Martin C. Weisskopf  <https://orcid.org/0000-0002-5270-4240>
 Kinwah Wu  <https://orcid.org/0000-0002-7568-8765>
 Silvia Zane  <https://orcid.org/0000-0001-5326-880X>
 Filippo Ambrosino  <https://orcid.org/0000-0001-7915-996X>
 Ruben Farinelli  <https://orcid.org/0000-0003-2212-367X>
 Andrea Gnarini  <https://orcid.org/0000-0002-0642-1135>
 Iván Agudo  <https://orcid.org/0000-0002-3777-6182>
 Lucio A. Antonelli  <https://orcid.org/0000-0002-5037-9034>
 Matteo Bachetti  <https://orcid.org/0000-0002-4576-9337>
 Luca Baldini  <https://orcid.org/0000-0002-9785-7726>
 Wayne H. Baumgartner  <https://orcid.org/0000-0002-5106-0463>
 Ronaldo Bellazzini  <https://orcid.org/0000-0002-2469-7063>
 Stefano Bianchi  <https://orcid.org/0000-0002-4622-4240>
 Stephen D. Bongiorno  <https://orcid.org/0000-0002-0901-2097>
 Raffaella Bonino  <https://orcid.org/0000-0002-4264-1215>
 Alessandro Brez  <https://orcid.org/0000-0002-9460-1821>
 Niccolò Bucciantini  <https://orcid.org/0000-0002-8848-1392>
 Fiamma Capitanio  <https://orcid.org/0000-0002-6384-3027>
 Simone Castellano  <https://orcid.org/0000-0003-1111-4292>
 Elisabetta Cavazzuti  <https://orcid.org/0000-0001-7150-9638>
 Chien-Ting Chen  <https://orcid.org/0000-0002-4945-5079>
 Stefano Ciprini  <https://orcid.org/0000-0002-0712-2479>
 Enrico Costa  <https://orcid.org/0000-0003-4925-8523>
 Alessandra De Rosa  <https://orcid.org/0000-0001-5668-6863>
 Ettore Del Monte  <https://orcid.org/0000-0002-3013-6334>
 Laura Di Gesu  <https://orcid.org/0000-0002-5614-5028>
 Niccolò Di Lalla  <https://orcid.org/0000-0002-7574-1298>
 Immacolata Donnarumma  <https://orcid.org/0000-0002-4700-4549>
 Victor Doroshenko  <https://orcid.org/0000-0001-8162-1105>
 Michal Dovčiak  <https://orcid.org/0000-0003-0079-1239>
 Steven R. Ehlert  <https://orcid.org/0000-0003-4420-2838>
 Teruaki Enoto  <https://orcid.org/0000-0003-1244-3100>
 Yuri Evangelista  <https://orcid.org/0000-0001-6096-6710>
 Sergio Fabiani  <https://orcid.org/0000-0003-1533-0283>
 Riccardo Ferrazzoli  <https://orcid.org/0000-0003-1074-8605>

Javier A. Garcia  <https://orcid.org/0000-0003-3828-2448>
 Shuichi Gunji  <https://orcid.org/0000-0002-5881-2445>
 Jeremy Heyl  <https://orcid.org/0000-0001-9739-367X>
 Wataru Iwakiri  <https://orcid.org/0000-0002-0207-9010>
 Svetlana G. Jorstad  <https://orcid.org/0000-0001-6158-1708>
 Vladimir Karas  <https://orcid.org/0000-0002-5760-0459>
 Fabian Kislat  <https://orcid.org/0000-0001-7477-0380>
 Jeffery J. Kolodziejczak  <https://orcid.org/0000-0002-0110-6136>
 Henric Krawczynski  <https://orcid.org/0000-0002-1084-6507>
 Luca Latronico  <https://orcid.org/0000-0002-0984-1856>
 Ioannis Lioudakis  <https://orcid.org/0000-0001-9200-4006>
 Simone Maldera  <https://orcid.org/0000-0002-0698-4421>
 Alberto Manfreda  <https://orcid.org/0000-0002-0998-4953>
 Frédéric Marin  <https://orcid.org/0000-0003-4952-0835>
 Alan P. Marscher  <https://orcid.org/0000-0001-7396-3332>
 Francesco Massaro  <https://orcid.org/0000-0002-1704-9850>
 Giorgio Matt  <https://orcid.org/0000-0002-2152-0916>
 Tsunefumi Mizuno  <https://orcid.org/0000-0001-7263-0296>
 Michela Negro  <https://orcid.org/0000-0002-6548-5622>
 Chi-Yung Ng  <https://orcid.org/0000-0002-5847-2612>
 Stephen L. O'Dell  <https://orcid.org/0000-0002-1868-8056>
 Nicola Omodei  <https://orcid.org/0000-0002-5448-7577>
 Chiara Oppedisano  <https://orcid.org/0000-0001-6194-4601>
 George G. Pavlov  <https://orcid.org/0000-0002-7481-5259>
 Abel L. Peirson  <https://orcid.org/0000-0001-6292-1911>
 Matteo Perri  <https://orcid.org/0000-0003-3613-4409>
 Melissa Pesce-Rollins  <https://orcid.org/0000-0003-1790-8018>
 Pierre-Olivier Petrucci  <https://orcid.org/0000-0001-6061-3480>
 Andrea Possenti  <https://orcid.org/0000-0001-5902-3731>
 Simonetta Puccetti  <https://orcid.org/0000-0002-2734-7835>
 Brian D. Ramsey  <https://orcid.org/0000-0003-1548-1524>
 Ajay Ratheesh  <https://orcid.org/0000-0003-0411-4243>
 Oliver J. Roberts  <https://orcid.org/0000-0002-7150-9061>
 Roger W. Romani  <https://orcid.org/0000-0001-6711-3286>
 Carmelo Sgrò  <https://orcid.org/0000-0001-5676-6214>
 Patrick Slane  <https://orcid.org/0000-0002-6986-6756>
 Paolo Soffitta  <https://orcid.org/0000-0002-7781-4104>
 Gloria Spandre  <https://orcid.org/0000-0003-0802-3453>
 Douglas A. Swartz  <https://orcid.org/0000-0002-2954-4461>
 Toru Tamagawa  <https://orcid.org/0000-0002-8801-6263>
 Fabrizio Tavecchio  <https://orcid.org/0000-0003-0256-0995>
 Roberto Taverna  <https://orcid.org/0000-0002-1768-618X>
 Nicholas E. Thomas  <https://orcid.org/0000-0003-0411-4606>
 Francesco Tombesi  <https://orcid.org/0000-0002-6562-8654>
 Alessio Trois  <https://orcid.org/0000-0002-3180-6002>
 Roberto Turolla  <https://orcid.org/0000-0003-3977-8760>
 Jacco Vink  <https://orcid.org/0000-0002-4708-4219>
 Fei Xie  <https://orcid.org/0000-0002-0105-5826>

References

- Abolmasov, P., Nättilä, J., & Poutanen, J. 2020, *A&A*, 638, A142
 Annala, E., Gorda, T., Katerini, E., et al. 2022, *PhRvX*, 12, 011058
 Arnaud, K. A. 1996, in ASP Conf. Ser. 101, *Astronomical Data Analysis Software and Systems V*, ed. G. H. Jacoby & J. Barnes (San Francisco: ASP), 17
 Baldini, L., Barbanera, M., Bellazzini, R., et al. 2021, *APh*, 133, 102628
 Baldini, L., Bucciantini, N., Lalla, N. D., et al. 2022, *SoftX*, 19, 101194
 Bellazzini, R., Spandre, G., Minuti, M., et al. 2006, *NIMPA*, 566, 552

- Bellazzini, R., Spandre, G., Minuti, M., et al. 2007, *NIMPA*, **579**, 853
- Calvelo, D. E., Fender, R. P., Tzioumis, A. K., & Broderick, J. W. 2012, *MNRAS*, **419**, L54
- Capitanio, F., Fabiani, S., Gnarini, A., et al. 2023, *ApJ*, **943**, 129
- Cocchi, M., Gnarini, A., Fabiani, S., et al. 2023, *A&A*, **674**, L10
- Connors, P. A., Piran, T., & Stark, R. F. 1980, *ApJ*, **235**, 224
- Connors, P. A., & Stark, R. F. 1977, *Natur*, **269**, 128
- Coriat, M., Fender, R. P., Tasse, C., et al. 2019, *MNRAS*, **484**, 1672
- Costa, E., Soffitta, P., Bellazzini, R., et al. 2001, *Natur*, **411**, 662
- D’Ai, A., Bozzo, E., Papitto, A., et al. 2012, *A&A*, **543**, A20
- Di Marco, A., Costa, E., Muleri, F., et al. 2022a, *AJ*, **163**, 170
- Di Marco, A., Muleri, F., Fabiani, S., et al. 2022b, *Proc. SPIE*, **12181**, 121811C
- Di Marco, A., Soffitta, P., Costa, E., et al. 2023a, *AJ*, **165**, 143
- Di Marco, A., La Monaca, F., Poutanen, J., et al. 2023b, *ApJL*, **953**, L22
- Doroshenko, V., Poutanen, J., Tsygankov, S. S., et al. 2022, *NatAs*, **6**, 1433
- Dovčiak, M., Karas, V., & Matt, G. 2004, *MNRAS*, **355**, 1005
- Fabiani, S., Capitanio, F., Iaria, R., et al. 2023, arXiv:2310.06788
- Farinelli, R., Fabiani, S., Poutanen, J., et al. 2023, *MNRAS*, **519**, 3681
- Fender, R., Spencer, R., Tzioumis, T., et al. 1998, *ApJL*, **506**, L121
- Fender, R., Wu, K., Johnston, H., et al. 2004, *Natur*, **427**, 222
- Gendreau, K. C., Arzoumanian, Z., Adkins, P. W., et al. 2016, *Proc. SPIE*, **9905**, 99051H
- Gnarini, A., Ursini, F., Matt, G., et al. 2022, *MNRAS*, **514**, 2561
- Harrison, F. A., Craig, W. W., Christensen, F. E., et al. 2013, *ApJ*, **770**, 103
- Hasinger, G., & van der Klis, M. 1989, *A&A*, **225**, 79
- Heinz, S., Schulz, N. S., Brandt, W. N., & Galloway, D. K. 2007, *ApJL*, **663**, L93
- Heinz, S., Sell, P., Fender, R. P., et al. 2013, *ApJ*, **779**, 171
- Iaria, R., Di Salvo, T., Robba, N. R., & Burderi, L. 2002, *ApJ*, **567**, 503
- Iaria, R., Spanò, M., Di Salvo, T., et al. 2005, *ApJ*, **619**, 503
- Iaria, R., Spanò, M., Di Salvo, T., et al. 2008, *ApJ*, **619**, 503
- Inogamov, N. A., & Sunyaev, R. A. 1999, *AstL*, **25**, 269
- Johnston, H. M., Fender, R., & Wu, K. 1999, *MNRAS*, **308**, 415
- Kaluzienski, L. J., Holt, S. S., Boldt, E. A., & Serlemitsos, P. J. 1976, *ApJL*, **208**, L71
- Kislat, F., Clark, B., Beilicke, M., & Krawczynski, H. 2015, *APh*, **68**, 45
- Linares, M., Watts, A., Altamirano, D., et al. 2010, *ApJL*, **719**, L84
- Loktev, V., Salmi, T., Nättilä, J., & Poutanen, J. 2020, *A&A*, **643**, A84
- Loktev, V., Veledina, A., & Poutanen, J. 2022, *A&A*, **660**, A25
- Madsen, K. K., Forster, K., Grefenstette, B., Harrison, F. A., & Miyasaka, H. 2022, *JATIS*, **8**, 034003
- Makishima, K., Maejima, Y., Mitsuda, K., et al. 1986, *ApJ*, **308**, 635
- Matsuoka, M., Kawasaki, K., Ueno, S., et al. 2009, *PASJ*, **61**, 999
- Miller-Jones, J. C. A., Moin, A., Tingay, S. J., et al. 2012, *MNRAS*, **419**, L49
- Mitsuda, K., Inoue, H., Koyama, K., et al. 1984, *PASJ*, **36**, 741
- Nasa Heasarc, 2014 HEASoft: Unified Release of FTOOLS and XANADU, Astrophysics Source Code Library, ascl:1408.004
- Nättilä, J., Miller, M. C., Steiner, A. W., et al. 2017, *A&A*, **608**, A31
- Popham, R., & Sunyaev, R. 2001, *ApJ*, **547**, 355
- Poutanen, J., Veledina, A., & Beloborodov, A. M. 2023, *ApJL*, **949**, L10
- Rankin, J., Muleri, F., Ferrazzoli, R., et al. 2023, *Proc. SPIE*, **12678**, 126780D
- Schulz, N. S., Kallman, T. E., Heinz, S., et al. 2019, *IAUS*, **346**, 125
- Schulz, N. S., Kallman, T. E., Heinz, S., et al. 2020, *ApJ*, **891**, 150
- Sell, P. H., Heinz, S., Calvelo, D. E., et al. 2010, *ApJL*, **719**, L194
- Shakura, N. I., & Sunyaev, R. A. 1988, *AdSpR*, **8**, 135
- Soffitta, P., Baldini, L., Bellazzini, R., et al. 2021, *AJ*, **162**, 208
- Soleri, P., Heinz, S., Fender, R., et al. 2009, *MNRAS*, **397**, L1
- Suleimanov, V., & Poutanen, J. 2006, *MNRAS*, **369**, 2036
- Sunyaev, R. A., & Titarchuk, L. G. 1985, *A&A*, **143**, 374
- Tennant, A. F., Fabian, A. C., & Shafer, R. A. 1986, *MNRAS*, **221**, 27P
- Titarchuk, L. 1994, Generalized comptonization models and application to the recent high energy observations, in AIP Conf. Proc. 304 (San Francisco, CA: ASP), **380**
- Titarchuk, L. 1994, *ApJ*, **434**, 570
- Tominaga, M., Tsujimoto, M., Ebisawa, K., Enoto, T., & Hayasaki, K. 2023, *ApJ*, **958**, 52
- Tudose, V., Fender, R. P., Tzioumis, A. K., Spencer, R. E., & van der Klis, M. 2008, *MNRAS*, **390**, 447
- Ursini, F., Farinelli, R., Gnarini, A., et al. 2023a, *A&A*, **676**, A20
- Ursini, F., Marinucci, A., Matt, G., et al. 2023b, *MNRAS*, **519**, 50
- van der Klis, M. 1989, *ARA&A*, **27**, 517
- Veledina, A., Muleri, F., Poutanen, J., et al. 2023, arXiv:2303.01174
- Viironen, K., & Poutanen, J. 2004, *A&A*, **426**, 985
- Weisskopf, M. C., Soffitta, P., Baldini, L., et al. 2022, *JATIS*, **8**, 026002
- Wilms, J., Allen, A., & McCray, R. 2000, *ApJ*, **542**, 914